



**HAL**  
open science

## Vibrational and electronic structures of tin selenide nanowires confined inside carbon nanotubes

Eric Faulques, Nataliya Kalashnyk, Charlotte Slade, Ana Sanchez, Jeremy Sloan, Victor Ivanov

► **To cite this version:**

Eric Faulques, Nataliya Kalashnyk, Charlotte Slade, Ana Sanchez, Jeremy Sloan, et al.. Vibrational and electronic structures of tin selenide nanowires confined inside carbon nanotubes. *Synthetic Metals*, 2022, 284, pp.116968. 10.1016/j.synthmet.2021.116968 . hal-03711853

**HAL Id: hal-03711853**

**<https://hal.science/hal-03711853v1>**

Submitted on 25 Aug 2022

**HAL** is a multi-disciplinary open access archive for the deposit and dissemination of scientific research documents, whether they are published or not. The documents may come from teaching and research institutions in France or abroad, or from public or private research centers.

L'archive ouverte pluridisciplinaire **HAL**, est destinée au dépôt et à la diffusion de documents scientifiques de niveau recherche, publiés ou non, émanant des établissements d'enseignement et de recherche français ou étrangers, des laboratoires publics ou privés.

# Vibrational and electronic structures of tin selenide nanowires confined inside carbon nanotubes

Eric Faulques<sup>\*,1</sup>, Nataliya Kalashnyk<sup>2</sup>, Charlotte A. Slade<sup>3</sup>, Ana M. Sanchez<sup>3</sup>, Jeremy Sloan<sup>3</sup> and Victor G. Ivanov<sup>4</sup>

Address: <sup>1</sup>University of Nantes, CNRS, Institut des Matériaux Jean Rouxel, IMN, F-44000 Nantes, France; <sup>2</sup>Laboratoire de Physique des Matériaux et des Surfaces, CY Cergy Paris University, Rue d'Eragny, Neuville sur Oise, F-95031 Cergy-Pontoise, France; <sup>3</sup>Department of Physics, University of Warwick, Gibbet Hill Road, Coventry CV4 7AL, United Kingdom and <sup>4</sup>Sofia University, Faculty of Physics, 5 James Bourchier Blvd., 1164 Sofia, Bulgaria

Email: Eric Faulques - eric.faulques@cnrs-imn.fr

\* Corresponding author

## Abstract

We study vibrational and electronic properties of tin selenide (SnSe) nanowires encapsulated in single walled carbon nanotubes (SWCNT) by combining experimental Raman spectroscopy and density functional theory (DFT) calculations at the Heyd-Scuseria-Ernzerhof (HSE) level. The theoretically investigated standalone SnSe nanowires are Sn<sub>4</sub>Se<sub>4</sub> with square (2×2) atomic arrangement and Sn<sub>6</sub>Se<sub>6</sub> with a repeating hexagonal Mo<sub>6</sub>S<sub>6</sub>-like structure. Raman data support the theoretical prediction that the square (2×2) nanowires possess specific modes at 151 and 185 cm<sup>-1</sup>, whereas the hexagonal Sn<sub>6</sub>Se<sub>6</sub> structure is characterized by a mode appearing at ~235 cm<sup>-1</sup>. Calculations predict that the (2×2) nanowire has an electronic gap of 1.5 eV and the Sn<sub>6</sub>Se<sub>6</sub> nanowire presents a semi-metallic character. Raman spectra of composite SnSe@SWCNT samples show that the radial breathing mode of the nanotubes is strongly suppressed indicating interaction between SWCNT and the encapsulated SnSe nanowire while the Fano asymmetry parameter of the *G* band is increased.

## 25 **Keywords**

26 carbon nanotubes, tin telluride, Raman spectroscopy, phonons, electrons, *ab-initio* calculations

## 27 **1 Introduction**

28 Inorganic and organic nanowires and nanostructured materials like nanorods or nanoplates are a  
29 topic of utmost importance in many studies of physics, chemistry, biology, and medicine. The me-  
30 chanical, electrical, electronic, magnetic, and chemical properties of these nano-objects can differ  
31 considerably from those of the parent bulk materials leading to applications for storage devices,  
32 electronic chips, photovoltaics, batteries, and therapeutic processes [1-7].

33 In particular, tin selenide, SnSe, is an important binary chalcogenide material which displays re-  
34 markable electronic, thermoelectric, and optoelectronic properties depending on its morphology  
35 as bulk crystal, thin films, or low-dimensional nanostructures [8]. This material can be applied no-  
36 tably for photovoltaics, anodes in rechargeable batteries, supercapacitors, phase-change memory  
37 devices, and topological insulators. Bulk tin(II) selenide is a narrow band-gap (IV-VI) semicon-  
38 ductor with both indirect and direct band gaps of 0.9 eV and 1.3 eV, respectively. The bulk chalc-  
39 genide crystal has an accordion-like stacked two-dimensional (2D) structure that gives it low an-  
40 harmonicity and low lattice thermal conductivity making it a poor thermal conductor while its ZT  
41 factor of merit has a high temperature value of 2.6 [9],[10].

42 Single-walled carbon nanotubes (SWCNT) are low-dimensional allotropes of carbon which have  
43 unique mechanical, electronic and optical properties depending on their morphology [11]. As  
44 expected for one-dimensional (1D) systems, they present van Hove singularities in the density of  
45 states whose energies vary with the diameter and length of the nanotube. Depending on their chi-  
46 rality SWCNTs are either metallic or semi-conductors allowing their application in flexible elec-  
47 tronic devices, lithium battery anodes, flat panel displays, sensors, supercapacitors, drug delivery,  
48 and STM/AFM tips [12,13]. Therefore, binary chalcogenides combined with SWCNTs can give  
49 rise to very unusual physical properties in the as-grown composites, but also this can foster drastic  
50 changes in the electronic properties of either component. Recently, several binary chalcogenides

51 have been encapsulated in both single-walled and double-walled carbon nanotubes (DWCNT) re-  
52 sulting in unique 1D chalcogenide crystalline wires with diameter comparable to a unit cell of the  
53 3D crystal [14-17]. Due to their extreme low lateral size and specific atomic arrangement, the phys-  
54 ical properties of these confined and atomically constrained nanowires are expected to be signifi-  
55 cantly different from those of the corresponding parent bulk materials.

56 Here we present a detailed comparative study of the structural, electronic, and vibrational prop-  
57 erties of two original nanostructures of atom-sized SnSe nanowires encapsulated in SWCNTs.

58 Previous high-resolution transmission electron microscopy (HRTEM) investigations have shown  
59 that SnSe crystallizes into  $(2 \times 2)$ -atom per cross section structure inside SWCNTs, adopting the  
60 same atomic arrangement as earlier described 1D  $(2 \times 2)$  KI nanocrystals, hereafter referred to as  
61  $\text{Sn}_4\text{Se}_4$ , embedded in double-walled or single-walled carbon nanotubes [14]. Recently, a novel 1D  
62 hexagonal SnSe crystalline form was discovered in SWCNTs [18] with an Mo(S,Se)-type of co-  
63 ordination environment [19,20], hereafter referred to as  $\text{Sn}_6\text{Se}_6$ , comprising three Sn atoms and  
64 three Se atoms per constituent layer, which is not observed in any of the other low-dimensional  
65 forms of the selenium chalcogenides. Interestingly, Nagata *et al.* [17] reported also similar MoTe  
66 nanowires structures in SWNTs. Previous DFT simulations predict a metallic nature of hexagonal  
67 MX nanowires with  $M=\text{Mo}, \text{W}$  and  $W=\text{S}, \text{Se}$  [21,22] but semiconducting properties for the isostruc-  
68 tural  $\text{Cr}_6\text{Te}_6$  compound [21]. Both, theoretical simulations and experiments, confirm the structural  
69 stability of the stand-alone Mo(S,Se) nanowires, which were found as effective nanoscale electri-  
70 cal connectors between  $\text{Mo}(\text{S}, \text{Se})_2$  monolayers [19,20]. In this aspect the physical properties of the  
71 isostructural Sn-based nanowires are far from understanding, and our work has been motivated by  
72 the following questions:

73 (i) Are the  $\text{Sn}_4\text{Se}_4$  and  $\text{Sn}_6\text{Se}_6$  nanowires structurally stable, or can they exist only encapsulated  
74 in SWCNTs?

75 (ii) Are the two types of nanowires semiconducting or metallic? While Carter *et al.* previously  
76 predicted a gaped band structure for  $\text{Sn}_4\text{Se}_4$  nanowire using different functional and pseu-

77 dopotentials [16], electronic properties of the then unobserved  $\text{Sn}_6\text{Se}_6$  1D crystal were not  
78 determined.

79 (iii) What are the vibrational modes of both  $\text{Sn}_4\text{Se}_4$  and  $\text{Sn}_6\text{Se}_6$  nanowires which could give sig-  
80 natures in Raman spectra of  $\text{SnSe@SWNT}$  composites? This question was not treated up to  
81 now.

82 (iv) What is the impact of encapsulation of the  $\text{SnSe}$  material on the physical properties of the  
83 surrounding nanotubes with matching diameter, e. g. metallic or semiconducting character ?

84 We addressed the first problems theoretically by means of extensive DFT calculations of the equi-  
85 librium structure, electronic band structure, and vibrational eigenmodes for the two forms of  $\text{SnSe}$   
86 nanowires. In order to assess the last two questions, we studied experimentally the Raman spec-  
87 tra of  $\text{SnSe@SWCNT}$  composites. Raman spectroscopy has proven to be a very efficient tool for  
88 characterizing SWCNTs embedding 1D atom-sized crystalline  $\text{HgTe}$  and  $\text{KI}$  nanowires [23,24]. In  
89 both cases it has been demonstrated that it is possible to identify several intrinsic vibrational modes  
90 of the nanowires superimposed with the Raman spectrum of SWCNTs. By following the same  
91 methodology here we study the in-situ dynamics of the embedded  $\text{SnSe}$  nanocrystals and their in-  
92 teractions with the nanotube walls. The radial breathing mode (RBM) and longitudinal vibrational  
93 modes ( $G$ -band) of the surrounding nanotubes are found to be strongly affected by the presence of  
94 the encapsulated material, which leads us to important conclusions concerning the electronic prop-  
95 erties of the  $\text{SnSe@SWCNT}$  composites corroborating the DFT predictions.

## 96 **2 Experimental methods and calculation details**

97 The  $\text{SnSe@SWCNT}$  samples were fabricated using infiltration protocols described previously  
98 [16,18]. In this set of experiments, commercial SWCNTs from NanoIntegris PureTubes (99%  
99 pure, 1.2-1.7 nm diameter, 300 nm to 5  $\mu\text{m}$  length) were used to encapsulate tin selenide. Here,  
100 the SWCNTs were washed, dissolved in  $N$ - Methyl-2-pyrrolidone (NMP), dried, pre-heated to  
101 1173 K to remove solvent and to open the tubes. The nanotubes were filled by the modified high

102 yield molten-phase capillarity technique adapted for SnSe filling. SWCNTs were intimately ground  
103 with SnSe (99.995%, Sigma Aldrich), and heated in pure silica quartz tubes sealed under vacuum  
104 to 100 K above the melting point of SnSe at around 1233 K.

105 Micro-Raman experiments were performed with Horiba Jobin-Yvon LabRAM HR 800 Vis and  
106 Renishaw inVia Reflex Raman microscope spectrometers in single monochromator mode with  
107 diffraction gratings of 600 and 1200 grooves/mm, respectively. Laser excitations  $\lambda_{\text{exc}} = 633$  and  
108 785 nm (1.96 and 1.58 eV) were provided by helium-neon and diode lasers, respectively. Spectra  
109 were collected at room temperature in the range between 100 and 3000  $\text{cm}^{-1}$  allowing the simulta-  
110 neous registration of the spectra of the fillers and the carbon nanotubes. The diameter and power of  
111 the laser spot on the sample surface were 2  $\mu\text{m}$ , 200  $\mu\text{W}$  (LabRAM) and 45  $\mu\text{W}$  (Renishaw) respec-  
112 tively, for the fully focused laser beam with 50 $\times$  objective magnification. The SnSe@SWCNT sam-  
113 ples were generally found to be homogeneous under microscope without the presence of significant  
114 amounts of extraneous SnSe amorphous or microcrystalline phase materials. Raman instruments  
115 were calibrated against the Stokes Raman signal of pure Si at 520.5  $\text{cm}^{-1}$  using a silicon wafer.  
116 The spectral resolution was 2  $\text{cm}^{-1}$ . In each experiment, several spectra were recorded on different  
117 spots in the samples. The Raman spectra of three characteristic composite SnSe@SWCNT sam-  
118 ples, # 1, # 2, and # 3 are presented and compared to those of SWCNT pristine samples.

119 The DFT calculations were performed with the Cambridge Serial Total Energy Package (CASTEP)  
120 plane wave code [25] by making use of Heyd-Scuseria-Ernzerhof screened Coulomb hybrid  
121 exchange-correlation functional HSE06 with 1/4 Hartree-Fock exchange [26] and norm-conserving  
122 pseudopotentials for the core electrons. The choice of this functional was motivated by a better  
123 geometry optimization of the  $\text{Sn}_6\text{Se}_6$  nanowire and calculation of the vibrational frequencies with-  
124 out imaginaries. It is also reported in the literature that HSE06 yields improved prediction of band  
125 gap energy and correct band structure in semiconductors [26]. HSE was also described to be well  
126 suited for calculating the phonon frequencies [26-29]. The plane-wave energy cutoff was set mainly  
127 at 440 eV (32.34 Ry), and in some cases at 350 and 400 eV. The self-consistent calculations for the  
128 1D  $\text{Sn}_4\text{Se}_4$  and  $\text{Sn}_6\text{Se}_6$  nanowires were performed on  $1 \times 1 \times 2$  and  $1 \times 1 \times 6$  Monkhorst-Pack

129 (MP) k-point mesh, respectively. We assessed the chosen DFT scheme by performing test calcula-  
130 tions for the bulk tin selenide on a  $1 \times 3 \times 3$  MP grid. Electronic convergence threshold for energy  
131 was set to be  $0.5 \times 10^{-6}$  eV. The optimization of cell parameters was allowed to proceed by keeping  
132 original symmetry with a total energy convergence tolerance of  $0.5 \times 10^{-5}$  eV/atom and until the  
133 force on each atom was less than 10 meV/Å. Phonon calculations were carried out at HSE level us-  
134 ing exclusively the finite displacement (FD) method in a supercell since the linear response scheme  
135 (Density Functional Perturbation Theory, DFPT) was not implemented with hybrid functionals in  
136 this DFT code.

### 137 **3 Results and discussion**

138 Experimental Raman spectra are discussed after the subsection of SnSe nanowires calculations.  
139 The spectra were recorded on several pristine and composite SWCNT samples. We sorted among  
140 these spectra those of three SnSe@SWCNT composites referred to as # 1, # 2, and # 3. They  
141 mainly differ from each other in the low frequency region characteristic of the RBM modes of the  
142 SWCNT molecular containers and of possible lines stemming from the SnSe encapsulated crystals.  
143 Spectra labelled # 0 are from the pristine SWCNT phase. Fig. 1 shows high-resolution transmission  
144 electron microscopy images (HRTEM) of the investigated SnSe filled samples. These images con-  
145 firm both the high filling fraction of SnSe in ‘NanoIntegris’ SWCNTs but also the composition of  
146 the encapsulated material.

#### 147 **3.1 Predictive calculations for stand-alone SnSe nanowires**

148 This section is devoted to the calculation and analysis of 1D SnSe nanowires. The final relaxed  
149 structures are given, and the phonons are calculated after geometry optimization. The  $\Gamma$ -point  
150 modes are classified with their different symmetries, and sorted by frequencies. Meanwhile, the  
151 electronic band structures of the standalone nanowires are presented and discussed.

### 152 3.1.1 Relaxed geometries

153 The geometries are entirely based on experimental HRTEM images realized on our samples [16,18]  
154 (see right panel in Fig. 1) and were chosen as those of infinite rods along the [001] direction rel-  
155 ative to a bulk cubic rocksalt unit cell with  $2\times 2$  and  $3+3$  SnSe cross sections, corresponding to  
156 square NaCl-like and hexagonal MoSe-like coordinations, respectively. The starting crystal pa-  
157 rameters of the  $\text{Sn}_4\text{Se}_4$  nanowire rely on HRTEM measurements by Carter *et al.* [16]. The initial  
158 distances in the hexagonal  $\text{Sn}_6\text{Se}_6$  nanowire were set arbitrarily at values close to those of the lay-  
159 ered *Pnma* bulk crystal with a translation period of  $c \sim 5 \text{ \AA}$  [30].

160 In order to perform the calculations with a plane wave (PW) basis set, periodic boundary condi-  
161 tions were imposed along the *a* and *b* axes of the nanowires with a period of  $10 \text{ \AA}$ . The geom-  
162 etry optimization of the nanowires converges to the two structures shown in Fig. 1. The opti-  
163 mized translation period *c* along the nanowire axis is  $5.708 \text{ \AA}$  and  $4.324 \text{ \AA}$  for  $\text{Sn}_4\text{Se}_4$  and  $\text{Sn}_6\text{Se}_6$   
164 nanowires, respectively. Some relevant interatomic distances for the two nanowires are shown in  
165 Fig. 1 and are listed in more detail in Table 1. Note that the Sn-Se distances of the  $\text{Sn}_6\text{Se}_6$  relaxed  
166 nanowire match well those found by Slade *et al.* in HRTEM images [18].

167 The rod symmetry elements of the two nanowires consist of a fourfold  $4_2$  or a sixfold  $6_3$  screw axis  
168 along *c*, of mirror planes *m* parallel to the *ab* and *bc* planes, an inversion center, and glide planes  
169 parallel to *ac* and *bc* planes with  $1/2$  translation of  $c/2$  (Fig. 1). Therefore, the  $\text{Sn}_4\text{Se}_4$  structure  
170 can be described by the rod symmetry group  $p4_2/mmc$  (No. 41) with all atoms occupying 4d Wyck-  
171 off positions. The  $\text{Sn}_6\text{Se}_6$  structure can be described as a periodic stack of equilateral  $\text{Sn}_3\text{Se}_3$  tri-  
172 angles. The triangles in the consecutive layers are rotated around the *c*-axis at  $180^\circ$  relative to each  
173 other, as shown in Fig. 1(c)-(d). Thus, the periodicity of the  $\text{Sn}_6\text{Se}_6$  structure corresponds to the  
174 doubled interlayer spacing, and the structure is described by the rod symmetry group  $p6_3/mmc$  (No.  
175 75) with all atoms occupying 6d Wyckoff positions.

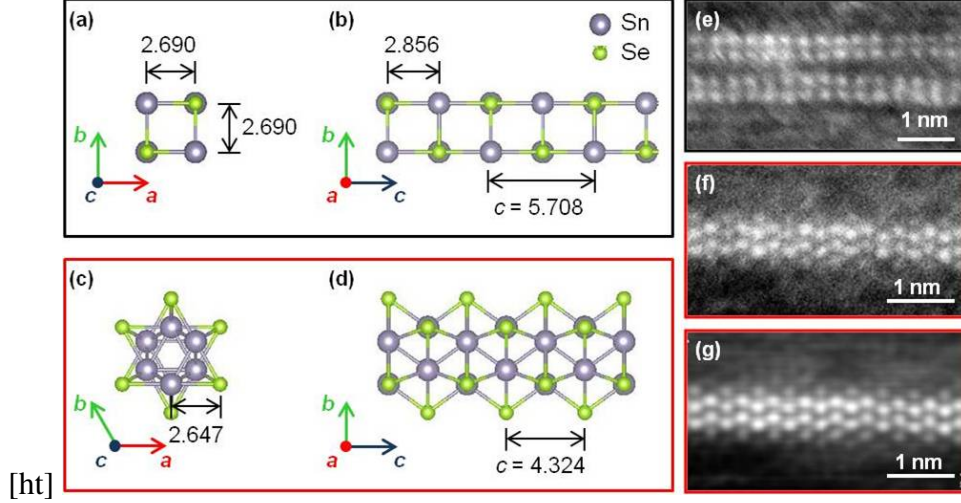


**Figure 1:** Left panel: Optimized structure of the two SnSe nanowires using the HSE hybrid functional. Vector  $\mathbf{c}$  is parallel to the nanowire axis. Vectors  $\mathbf{a}$  and  $\mathbf{b}$  represent the translation periods of the surrounding superlattice and are parallel to the SnSe layers. All distances are in Angstroms. The  $2 \times 2$  SnSe crystal of  $p4_2/mmc$  symmetry: views along the nanowire axis (a) and parallel to the  $\text{Sn}_2\text{Se}_2$  layers (b). The hexagonal  $\text{Sn}_6\text{Se}_6$  crystal of  $p6_3/mmc$  symmetry: views along the nanowire axis (c) and parallel to the  $\text{Sn}_3\text{Se}_3$  layers (d). Right panel: (e) experimental HRTEM annular dark field (ADF) image of a pair of  $2 \times 2$  SnSe crystals observed in a representative SWCNT sample; (f) and (g) unfiltered and adaptive filtered ADF images of an encapsulated  $\text{Sn}_6\text{Se}_6$  crystal observed in the same representative SWCNT sample.

### 176 3.1.2 Normal modes of vibrations

177 The normal modes of vibrations were calculated for the optimized structures at the  $\Gamma$ -point and  
 178 along the  $\Gamma - Z$  direction for the  $\text{Sn}_4\text{Se}_4$  nanowire. A one-dimensional acoustic sum rule was im-  
 179 posed on the dynamical matrix in order to account for the four zero-frequency modes of a freely  
 180 standing nanowire: the three free translations and also the free rotation about the  $c$  axis. Since the  
 181 unit cells of the  $\text{Sn}_4\text{Se}_4$  and  $\text{Sn}_6\text{Se}_6$  nanowires contain 8 and 12 atoms respectively, their corre-  
 182 sponding phonon spectra consist of 24 and 36 dispersion branches along the  $\Gamma$ -Z direction. The  
 183 normal modes of the  $\text{Sn}_4\text{Se}_4$  and  $\text{Sn}_6\text{Se}_6$  nanowire at the  $\Gamma$ -point are classified according to the  
 184 irreducible representations of the  $4/mmm$  ( $D_{4h}$ ) and  $6/mmm$  ( $D_{6h}$ ) point groups. The symmetry de-  
 185 composition was performed with the aid of SAM software available on the Bilbao Crystallographic  
 186 Server [31]. The mechanical representations are:

$$187 \Gamma_{22} = 2A_{1g} + 2A_{2g} + 2B_{1g} + 2B_{2g} + 2E_g + 2A_{2u} + 2B_{2u} + 4E_u \quad (1)$$

**Table 1:** Optimized structure parameters of Sn<sub>4</sub>Se<sub>4</sub> and Sn<sub>6</sub>Se<sub>6</sub> standalone nanowires calculated with HSE06 hybrid functional. The bond lengths between atoms belonging to the same Sn<sub>2</sub>Se<sub>2</sub> (Sn<sub>3</sub>Se<sub>3</sub>) plane are denoted as “in”, and those between atoms from neighboring planes – by “out”.

Sn <sub>2</sub> Se <sub>2</sub>	Distance (Å)
Translation period <i>c</i>	5.708
Sn–Se (in)	2.690
Sn–Sn (in)	3.698
Se–Se (in)	3.909
Sn–Se (out)	2.856

[h]

Sn <sub>6</sub> Se <sub>6</sub>	Distance (Å)
Translation period <i>c</i>	4.324
Sn–Se (in)	2.647
Sn–Sn (in)	2.698
Se–Se (in)	2.668
Sn–Se (out)	2.664

188 for the Sn<sub>4</sub>Se<sub>4</sub> SnSe nanowire, and

$$\begin{aligned}
 \Gamma_{33} = & 2A_{1g} + 2A_{2g} + 2B_{2g} + 2E_{1g} + 4E_{2g} + 2A_{2u} + 2B_{1u} \\
 & + 2B_{2u} + 4E_{1u} + 2E_{2u}
 \end{aligned}
 \tag{2}$$

190 for the Sn<sub>6</sub>Se<sub>6</sub> hexagonal nanowire. The acoustic modes are  $A_{2u} + E_u$  and  $A_{2u} + E_{1u}$  for the Sn<sub>4</sub>Se<sub>4</sub>  
191 and Sn<sub>6</sub>Se<sub>6</sub> nanowires, respectively. The near-zero-frequency rigid rotations about *c* of the Sn<sub>4</sub>Se<sub>4</sub>  
192 and Sn<sub>6</sub>Se<sub>6</sub> wires correspond to modes of  $A_{2g}$  symmetry. The other  $A_{2g}$  and  $B_{2u}$  modes in the  
193 Sn<sub>4</sub>Se<sub>4</sub> nanowire, as well as the  $A_{2g}$ ,  $B_{2g}$ ,  $B_{1u}$ ,  $B_{2u}$ , and  $E_{2u}$  modes in the Sn<sub>6</sub>Se<sub>6</sub> nanowire are op-  
194 tically silent. The remaining even (g) modes are Raman active:

$$\Gamma_{22\text{Raman}} = 2A_{1g} + 2B_{1g} + 2B_{2g} + 2E_g \tag{3}$$

$$\Gamma_{33\text{Raman}} = 2A_{1g} + 2E_{1g} + 4E_{2g} \tag{4}$$

198 while the rest of the odd (u) modes possess infrared (IR) activity:

$$\Gamma_{22\text{IR}} = A_{2u} + 3E_u \quad (5)$$

$$\Gamma_{33\text{IR}} = A_{2u} + 3E_{1u} \quad (6)$$

Therefore, accounting for the degeneracy of the representations, eight different frequencies are expected in the Raman spectra of both nanowires. The corresponding number of the infrared active modes is four in the two structures. The calculated frequencies of the  $\Gamma$ -point modes are summarized in Table 2.

In  $\text{Sn}_4\text{Se}_4$  and  $\text{Sn}_6\text{Se}_6$  nanowires the  $A_{1g}$  and the  $E_g$  ( $E_{1g}$ ) vibrations entail comparable types of atomic displacements. The totally symmetric  $A_{1g}$  modes are radial breathing-type modes of the Sn and Se sublattices. The  $E_g$  ( $E_{1g}$ ) modes involve atomic motions along the nanowire axis, and can be defined as shearing deformations of the two atomic sublattices. Table 2 gives the calculated  $\Gamma$ -point vibrational frequencies for the standalone  $\text{Sn}_4\text{Se}_4$  and  $\text{Sn}_6\text{Se}_6$  nanowires. The modes of the same symmetry are numbered in an ascending order of their frequencies.

### 3.1.3 Electronic band structures

Fig. 2 presents the electronic band structures, as well as the full and partial density of states (DOS) calculated with the HSE06 functional for the layered SnSe bulk crystal and the  $\text{Sn}_4\text{Se}_4$  and  $\text{Sn}_6\text{Se}_6$ -embedded nanowires. Zero energy corresponds to the Fermi energy  $E_F$ .

Note that in periodic DFT calculations, the 1D nanowire is placed in the center of a vacuum box of dimensions  $a, b, c$  with volume  $V$  sufficiently large to neglect inter-wires interactions. In this 3D scheme, the DOS for electrons or phonons of the wire at energy  $E$  can be written as:

$$\rho_{3D}(E) = \frac{V}{(2\pi)^3} \int_{-\pi/a}^{\pi/a} \int_{-\pi/b}^{\pi/b} \int_{-\pi/c}^{\pi/c} dk_x dk_y dk_z \delta(E - E(\mathbf{k})) \quad (7)$$

Provided that the interaction between periodic replica of the nanowire is negligible, the band energy function  $E(\mathbf{k})$  is practically dispersionless in the  $xy$ -plane, i.e.  $E(k) \equiv E(k_z)$ , where  $k_z$  is the

222 1D wavevector along the nanowire axis. In this case the equation (7) is transformed into equivalent  
 223 expression for the 1D density of states of the nanowire:

$$224 \quad \rho_{1D}(E) = \frac{c}{2\pi} \int_{-\pi/c}^{\pi/c} dk_z \delta(E - E(k_z)) \quad (8)$$

225 Therefore, the  $\rho_{1D}$  values discussed hereafter depend only on translation period  $c$  of the wire and  
 226 are in principle independent of the vacuum box dimension.

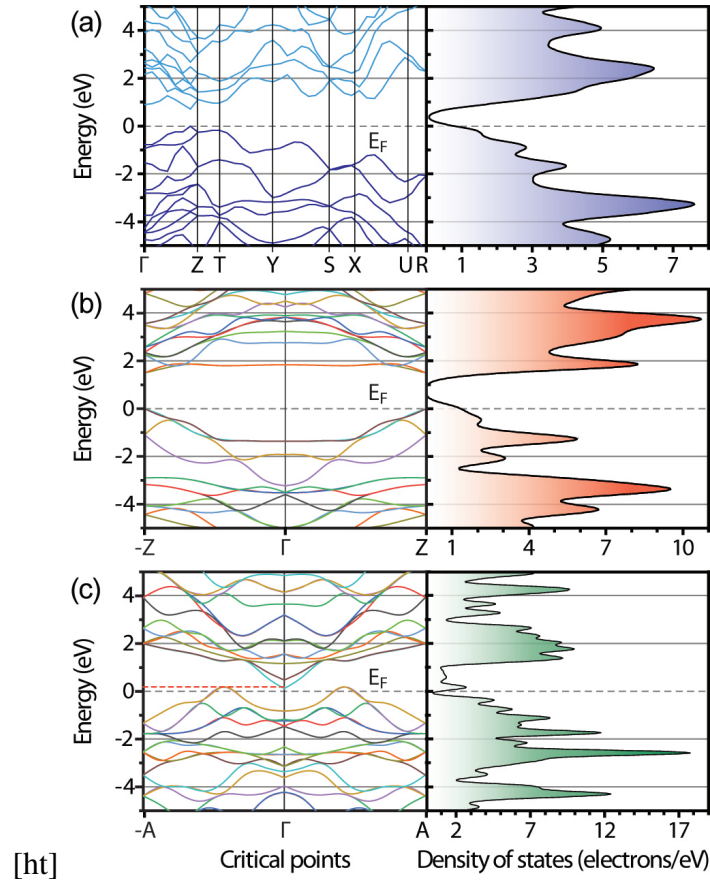


**Figure 2:** Band structures and density of states of SnSe crystals calculated with DFT at HSE06 level. (a) 3D  $Pnma$  crystal; (b) 1D square  $\text{Sn}_4\text{Se}_4$  nanowire along  $-Z\Gamma Z$  direction; (c) 1D hexagonal  $\text{Sn}_6\text{Se}_6$  nanowire along  $-A\Gamma A$  directions with spline interpolation. A semimetallic character is revealed above the Fermi level (dotted line).  $\Gamma Z$  and  $\Gamma A$  paths are oriented along the chain direction. The critical points Z and A lie at the edge of the Brillouin zone with coordinate  $(0,0,1/2)$ . The electronic configuration of Sn atom is  $[\text{Kr}]5s^24d^{10}5p^2$ , s and p orbitals hold valence electrons ( $n = 5$ ).

227 The band gap in the layered 3D  $Pnma$  crystal is 0.71 eV, a value relatively close to the experimental

228 indirect band gap (0.9 eV) and is in the same range as values reported in previous works [32]. The  
229 band structure of the  $\text{Sn}_4\text{Se}_4$  nanowire clearly evidences a direct band gap of 1.49 eV at Z point  
230 which should allow optical and resonant transitions in the near IR at about 830 nm. This bandgap  
231 energy is higher than those of the *Pnma* crystal (indirect : 0.9 eV, direct : 1.3 eV) and closer to that  
232 found by Carter *et al.* [16] for the same infinite rod (1.36 eV) when using the PW91 functional.  
233 These two DFT calculations stress that the infinite  $\text{Sn}_4\text{Se}_4$  nanorod should present a band gap ex-  
234 pansion with respect to the bulk layered form.

235 Here, computations at PBE and HSE levels of theory show that the  $\text{Sn}_6\text{Se}_6$  nanowire has an almost  
236 gapless electronic structure with a small nonzero density of states at the Fermi level. For HSE06  
237 the upper valence branch crosses the Fermi level with a valence band maximum (VBM) at 0.18  
238 eV above  $E_F$  while the conduction band minimum (CBM) is only 0.11 eV above  $E_F$  at the  $\Gamma$  point  
239 (Fig. 2(c)). These VBM and CBM values indicate an energy overlap of about 70 meV suggesting  
240 that the  $\text{Sn}_6\text{Se}_6$  nanowire is a semimetal. To support this prediction, it should be noticed than Yan  
241 *et al.* [33] have observed a semiconductor to semimetal transition in powdered SnSe at a pressure  
242 of 9 GPa, which has been also verified by their GGA-PBE band structure calculations. The elec-  
243 tronic calculations of Yan *et al.* at 9 GPa in the  $\Gamma Z$  direction ( $Z: (0,0,1/2)$ ) show the same behavior  
244 found in the  $\text{Sn}_6\text{Se}_6$  nanowire: the upper valence band crosses the Fermi level while the lower con-  
245 duction band goes down to almost zero energy at  $\Gamma$  point.

### 246 **3.2 Additional Raman bands upon SnSe encapsulation**

247 Fig. 3 presents the unpolarized micro-Raman spectra of a pristine SWCNT sample # 0 and  
248  $\text{SnSe@SWCNT}$  sample # 1 between 100 and 3000  $\text{cm}^{-1}$  obtained at excitation wavelength 785  
249 nm (1.58 eV) for the same power density. In SWCNT spectrum the band of RBM modes is strongly  
250 resonant with maximum intensity close to that of the *G* band. The *G* band exhibits an asymmet-  
251 ric shape characteristic of metallic nanotubes contribution and has three components at 1556,  
252 1571, and 1592-1595  $\text{cm}^{-1}$  stemming from both metallic (M) and semiconducting (SC) tubes re-

253 spectively referred to as  $G^-$  (LO phonon of M tubes),  $G^+$  (TO phonon of SC tubes), and  $G^+$  (LO  
254 phonon of SC tubes) [34,35].

255 Fig. 4 shows that the RBM frequencies of the pristine nanotubes appear between 150 and 180  $\text{cm}^{-1}$   
256 with two resolved peaks at 163 and 173  $\text{cm}^{-1}$ . The spectra are normalized to the maximum Raman  
257 intensity of low frequency lines for clarity.

258 Applying the empirical relationship between the RBM frequency in  $\text{cm}^{-1}$  and tube diameter  $d$  [35],  
259  $d(\text{nm}) = 227/\omega_{\text{RBM}}$ , we estimate that these peaks are characteristic for SWCNTs of 1.4 nm and  
260 1.3 nm diameter, respectively. Thus the experimental Raman results confirm that the commercial  
261 nanotubes of 1.2-1.7 nm diameter range chosen for the synthesis of our composites are the dom-  
262 inant crystalline structural forms in the samples analyzed here, notwithstanding that other forms  
263 may possibly exist but they were not extensively encountered in our study. These diameters can  
264 easily accommodate the two types of SnSe 1D nanocrystals discussed in this paper. The estimated  
265 diameter of SWCNTs surrounding the SnSe nanowires is:

$$266 \quad d = d(\text{Se-Se}) + 2r_{\text{vdW}}(\text{Se}) + 2r_{\text{vdW}}(\text{C}) \quad (9)$$

267 where  $r_{\text{vdW}}$  is the van der Waals radius of the atom and  $d(\text{Se-Se})$  is the cross-sectional distance  
268 between opposite Se atoms. For optimized geometries of  $\text{Sn}_4\text{Se}_4$  and  $\text{Sn}_6\text{Se}_6$  crystals we find  $d =$   
269 1.11 nm and 1.45 nm, respectively. These values correspond well with the diameter estimates from  
270 Raman spectra.

271 Strikingly several novel lines appear at low frequencies in the Raman spectra of SnSe@SWCNT  
272 samples # 1, # 2 and # 3 for exciting wavelengths 633 and 785 nm, while the absolute intensity of  
273 the RBM and  $G$  modes either vanishes or strongly diminishes.

274 These additional low-frequency bands are located at 108-109, 126-131, 151, 185, 235  $\text{cm}^{-1}$  (see  
275 Fig. 3 and Fig. 4). All these bands are absent in the pristine nanotubes spectrum (samples # 0). For  
276 sample # 1 the signals of nanotube walls are hardly detected in the region between 140 and 180  
277  $\text{cm}^{-1}$  and are overlapped by the additional band at 150  $\text{cm}^{-1}$ . In sample # 2, the RBM bands are  
278 absent.

279 The supplemental lines appearing for the SnSe@SWCNT samples may result from encapsula-  
280 tion of SnSe in SWCNTs since their relative intensities do not match those of bulk *Pnma* SnSe or  
281  $P\bar{3}m1$  SnSe<sub>2</sub> crystals at 111 cm<sup>-1</sup> (*E<sub>g</sub>*) and at 187 cm<sup>-1</sup> (*A<sub>1g</sub>*) as shown in Fig. 4, and therefore do  
282 not seem characteristic of remnant tin selenide compounds in between and outside the nanotubes  
283 walls [36-41]. It can be inferred that these bands are likely to characterize mainly other phases of  
284 tin selenide. This assumption is supported by the changes of the RBM and *G* bands of the SWC-  
285 NTs in the SnSe@SWCNT nanostructures. The relative intensity of these lines and their moder-  
286 ate HWHM indicate that these crystals are well ordered inside the SWCNT walls. The additional  
287 strong bands at 185 and 235 cm<sup>-1</sup> cannot be ascribed to the SnSe *Pnma* crystal. We found that for  
288 633 nm excitation this compound exhibits Raman bands at 32 (*A<sub>g</sub>*), 55 (*B<sub>1g</sub>*), 68 (*A<sub>g</sub>*), 106 (*B<sub>3g</sub>*),  
289 129 (*A<sub>g</sub>*), 148 (*A<sub>g</sub>*), and 179 cm<sup>-1</sup> (very weak) in agreement with previous work [36]. They likely  
290 characterize intrinsic features of the nanowires embedded in SWCNT because the occurrence of  
291 these bands is predicted in SnSe 1D standalone crystals by the vibrational calculations described  
292 hereafter. Our interpretation is also conformed by Raman data of MoTe@SWNT samples acquired  
293 by Nagata *et al.* [17]. They found in their samples a Raman line at 255 cm<sup>-1</sup> that they ascribed to  
294 the vibrations of the embedded MoTe nanowires. Similarly to our experiments, their observation  
295 was carried out at a laser power of 347 μW using the same equipment and the He-Ne 633 nm laser  
296 line. Since Sn<sub>6</sub>Se<sub>6</sub> and MoTe nanowires have close structures, their Raman experiment suggests  
297 that the SnSe nanowires vibrational Raman lines should lie in the same range of frequencies.

### 298 **3.3 Analysis of *G* bands**

299 At higher frequencies the *G*<sup>-</sup>, *G*<sup>+</sup> modes of the SnSe@SWCNT samples are still visible but are  
300 considerably reduced in intensity (Fig. 3). The profile of the *G* band remains strongly asymmetric  
301 with a shift of the two *G*<sup>+</sup> components towards higher energies by about 4 cm<sup>-1</sup> at 1578, and 1596  
302 cm<sup>-1</sup>, respectively (blueshift). There is an overall diminution of the spectral signal-to-noise ratio  
303 in samples # 1 and # 2 and the relative intensity of the *G*<sup>+</sup> TO line located at 1578 cm<sup>-1</sup> is weaker.  
304 The relative intensity of the *D* band is enhanced with respect to that of *G* band indicating that more

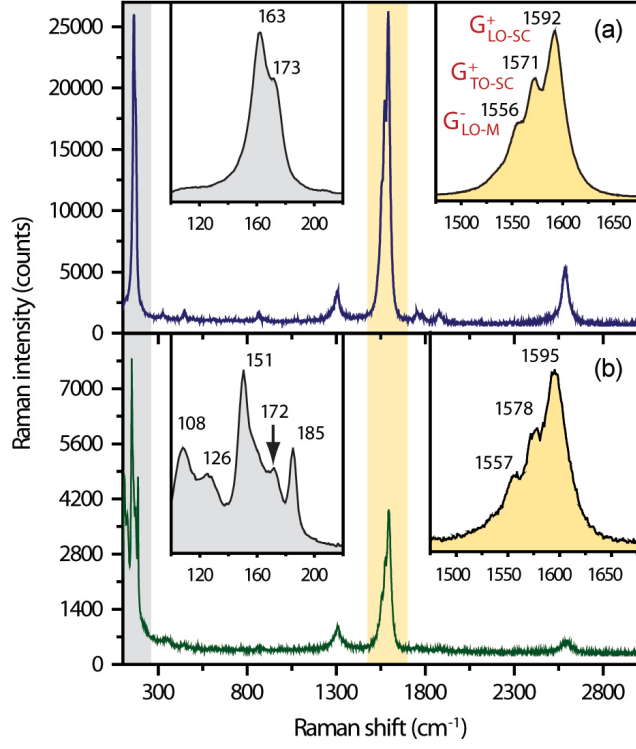


**Figure 3:** Experimental Raman spectra of pristine SWCNT (NanoIntegris 99% pure sample # 0), a), and SnSe@SWCNT sample # 1, b) recorded between 100 and 3000  $\text{cm}^{-1}$  at excitation 1.58 eV (785 nm) and for the same laser power. The insets show sub-band features in the  $G$  band for pristine sample and RBM frequency region for the composite.

305 defects are present in the encapsulating nanotube walls. Finally, the second order  $G'$  ( $2D$ ) band lo-  
 306 cated at  $2586 \text{ cm}^{-1}$  in pristine SWCNTs shifts towards  $2600 \text{ cm}^{-1}$  and weakens in relative intensity  
 307 in the SnSe@SWCNT samples. The blueshift of the  $G$  and  $G'$  Raman bands upon encapsulation of  
 308 SnSe and the overall intensity damping of the spectrum indicates a  $p$ -type doping of the SWCNT  
 309 template [42,43].

310 This experimental result is in line with DFT calculations of work functions (WF) carried out on the  
 311 SnSe standalone nanowires and presented in the Supporting Information. For  $\text{Sn}_4\text{Se}_4$ , the bonding  
 312 energies of HOMO (4.574 eV) and LUMO (3.385 eV) are lower than the known WF of SWCNT  
 313 ( $\sim 4.8$  eV) and near the WF of graphene (4.6 eV). The calculated WF of  $\text{Sn}_4\text{Se}_4$ , which refers to  
 314 the Fermi level situated in the middle between HOMO and LUMO, is 3.98 eV. Thus, if there is  
 315 a charge transfer between the  $\text{Sn}_4\text{Se}_4$  and the SWCNT, the CNT should accept electrons, i.e. be-  
 316 come  $n$ -doped. However, the calculated WF of  $\text{Sn}_6\text{Se}_6$  is 5.412 eV, significantly larger than that of

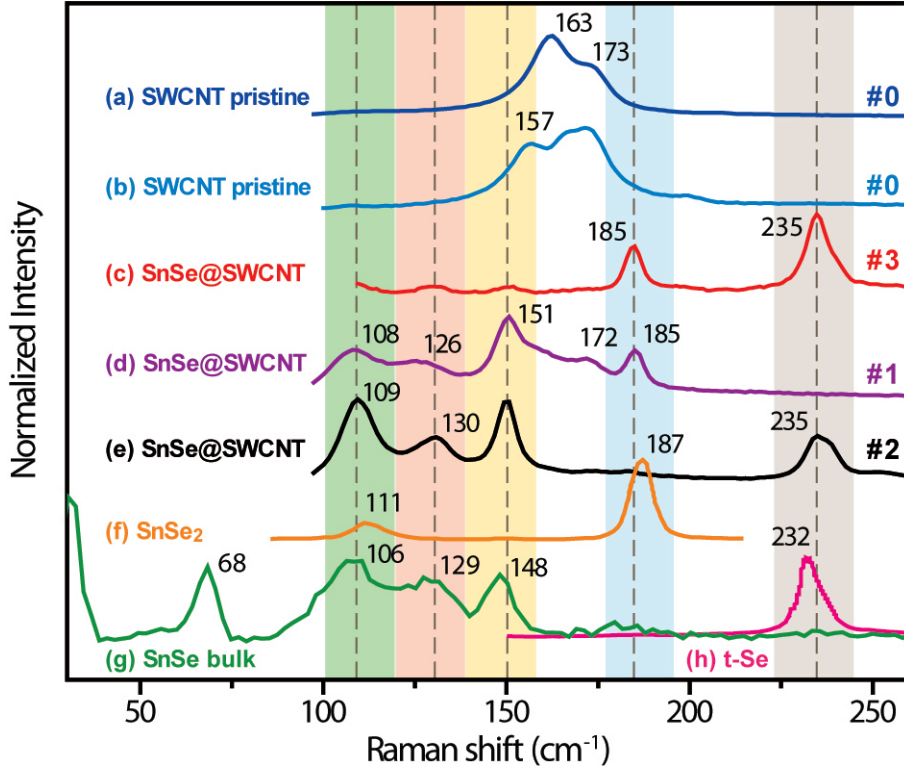


**Figure 4:** Low frequency Raman spectra of pristine SWCNT, SnSe filled SWCNT, and tin selenide compounds. Pristine SWCNT sample # 0 (NanoIntegris 99% pure) at  $\lambda_{exc} = 785 \text{ nm}$  (1.58 eV) (a) and  $\lambda_{exc} = 633 \text{ nm}$  (1.96 eV) (b); (c) SnSe@SWCNT (sample # 3)  $\lambda_{exc} = 633 \text{ nm}$ ; (d,e) SnSe@SWCNT (samples # 1 # 2),  $\lambda_{exc} = 785 \text{ nm}$ ; (f) SnSe<sub>2</sub>  $P\bar{3}m1$  crystal,  $\lambda_{exc} = 785 \text{ nm}$ ; (g) SnSe  $Pnma$  crystal  $\lambda_{exc} = 633 \text{ nm}$ ; (h) for information: trigonal Se  $P3_121$  crystal,  $\lambda_{exc} = 633 \text{ nm}$ . Spectra (f,h) are taken from literature.

317 SWCNT. Therefore, in this case we can rationalize that the CNT should oppositely give electrons to  
 318 the Sn<sub>6</sub>Se<sub>6</sub> nanowire, i.e. be *p*-doped. Thus the spectral signatures of a *p*-doping (or hole doping)  
 319 of SWCNTs could be fingerprints for presence of Sn<sub>6</sub>Se<sub>6</sub> nanowires encapsulated in the nanotubes.  
 320 One can anticipate that the experimental shape of the *G* band can be fitted by adding together two  
 321 Lorentzian functions for *G*<sup>+</sup> LO and *G*<sup>+</sup> TO lines and a Breit-Wigner-Fano (BWF) line shape for  
 322 the *G*<sup>-</sup> LO sub-band [44]. This choice is supported by the fact that the *G*<sup>-</sup> LO sub-band is sup-  
 323 posed to stem from the tangential vibrational modes of metallic SWCNTs [45] and therefore may  
 324 acquire a BWF profile. By theoretical predictions Gayen *et al.* [46] also anticipated that a BWF  
 325 lineshape might be observed on the *G* band when semiconducting SWNTs are filled with donor

326 atoms. The BWF lineshape writes as:

$$327 \quad I(\omega) = \frac{I_0 [1 + (\omega - \omega_{BWF})/q\Gamma]^2}{1 + [(\omega - \omega_{BWF})/\Gamma]^2} \quad (10)$$

328 where  $I_0$  is the maximum intensity of the line,  $\omega_{BWF}$  the resonance frequency,  $\Gamma$  the spectral width,  
329 and  $1/q$  the asymmetry parameter.

330 Fig. 5 shows the experimental Raman spectra fitted with a Breit-Wigner-Fano and two Lorentzians  
331 functions obtained for pristine SWCNT (sample # 0), and the two SnSe@SWCNT samples (# 1 and  
332 # 2) presented above. Several modifications of the Raman spectra occur upon encapsulation (see  
333 Fig. 5):

334 (i) The three components of the tangential  $G$  band features undergo both shape and energy changes.  
335 The BWF component corresponding to the  $G^-$  LO mode of metallic tubes is more asymmetric with  
336 an upshift of about  $2 \text{ cm}^{-1}$ . The Lorentzian components  $G^+$  TO and  $G^+$  LO of semiconducting  
337 tubes are upshifted by 3 to  $4 \text{ cm}^{-1}$ , and their FWHM increases.

338 (ii) The integrated intensity ratio of BWF and highest Lorentzian components ( $I_{BWF}/I_{G^+LO}$ ) dimin-  
339 ishes after encapsulation due to the broadening of the  $G^+$  LO feature.

340 (iii) The asymmetry parameter  $|1/q|$  is much higher for encapsulating samples than for the pristine  
341 sample indicating that metallicity of tubes is increased in these nanomaterials as expected from the  
342 calculated band structures. The value found after fitting for pristine SWCNT is 0.196, close to that  
343 of Ref. [44] (0.23) while for samples # 1 and # 2, it increases to 0.380, and 0.306, respectively.

344 The interference part of the BWF profile in eq. 11, i.e. the BWF interference function [47], is ex-  
345 pressed as

$$346 \quad I'(\omega) = \frac{2(\omega - \omega_{BWF})/q\Gamma}{1 + [(\omega - \omega_{BWF})/\Gamma]^2} \quad (11)$$

347 It characterizes the interaction between the vibrational mode and a constant continuum of elec-  
348 tronic excitations. A plot of this function shows that the electron-phonon interaction between  $G^-$

349 LO and  $G^+$  TO Raman contributions in the encapsulating samples is stronger, showing that metal-  
350 licity of these samples is higher than in the pristine carbon nanotubes.

351 In addition, the difference of interference functions between SnSe@ SWCNT and pristine SWCNT  
352 samples indicates that a stronger BWF interaction occurs in the former as exemplified by Fig. 5(b)  
353 (red contour) whose signal is positive in the range 1540-1565  $\text{cm}^{-1}$  and whose maximum is located  
354 near the frequency of the BWF component in SWCNT (1555  $\text{cm}^{-1}$ ) and SnSe@SWCNT samples.

355 As a consequence, the BWF interference does not affect the  $G^+$  LO mode in SnSe@SWCNT but  
356 may have a small influence on the frequency of the  $G^+$  TO mode. Overall, the frequency hardening  
357 of the  $G^-$  band between pristine and encapsulating nanotubes is mainly due to the encapsulated  
358 crystals modifying the mechanical properties of the nanotubes walls.

359 In a previous work, CNTs have been decorated by SnSe crystals for applications in Li-battery elec-  
360 trodes [48]. In this case there no encapsulation of the chalcogenide. Raman spectra recorded on  
361 these hybrids exhibit  $D$  and  $G$  band profiles different than those we have observed in this work.

362 Aside our HRTEM investigation, this is a hint that the CNTs in our samples are not covered by the  
363 chalcogenide.

### 364 **3.4 Phonons of the encapsulated nanowires**

365 The phonon dispersions and DOS have been calculated at HSE level of theory for the two SnSe  
366 standalone nanowires and for the  $Pnma$  SnSe crystal for comparison (Fig. 6). Additionally, the par-  
367 tial phonon DOS unveils the individual contribution of Sn and Se atoms to the vibrational spec-  
368 trum.

369 The partial phonon DOS of the SnSe  $Pnma$  crystal shows that the main Sn vibrations occurring be-  
370 tween 60-72  $\text{cm}^{-1}$ , accompanied by additional modes at 176 and 194  $\text{cm}^{-1}$ , with small densities at  
371 109 and 210  $\text{cm}^{-1}$ . The Se vibrations are mainly centered at 180 and 194  $\text{cm}^{-1}$  with smaller densi-  
372 ties at 59, 70, 108 and 209  $\text{cm}^{-1}$ .

373 The partial DOS of the  $\text{Sn}_4\text{Se}_4$  nanowire reveal strong differences with the 3D bulk crystal. The  
374 DOS exhibit more featured spectra with large contributions at 30, 54, 72, 96, 113, 149, 192  $\text{cm}^{-1}$

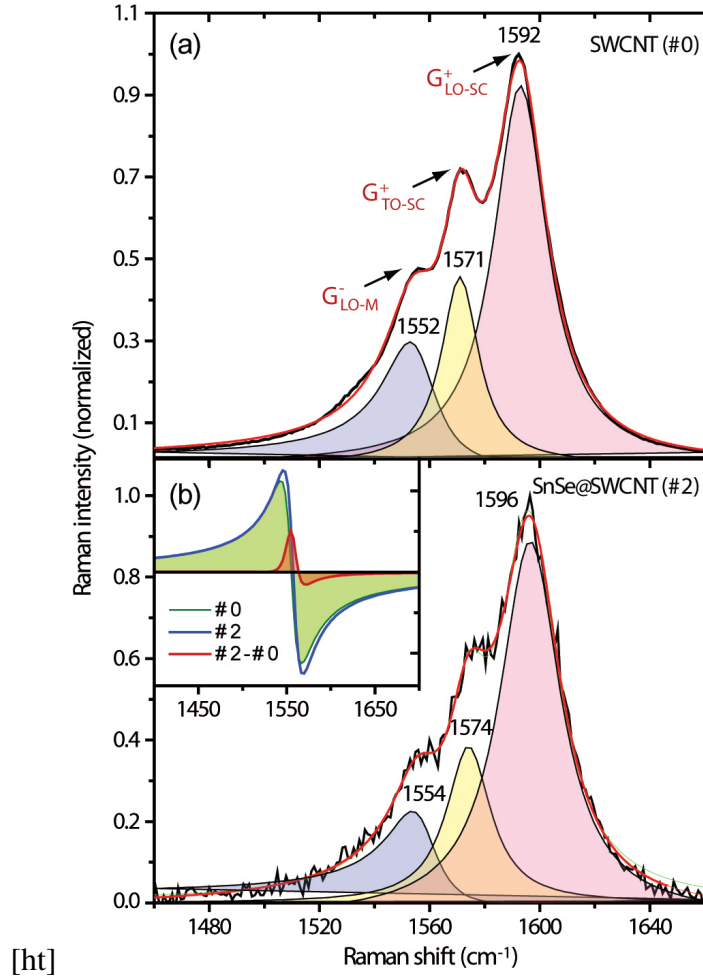


**Figure 5:** Normalized experimental Raman spectra of pristine and SnSe filled SWCNT fitted with a BWF function ( $G^-$  band) and two Lorentzian functions ( $G^+$  TO and  $G^+$  LO bands). (a): pristine SWCNT (NanoIntegriss 99% pure, sample # 0). (b): SnSe@SWCNT (sample # 2). In inset: BWF interference functions for SWCNT (green contour), sample # 2 (solid blue line), and differences of BWF interference functions between sample # 2 and SWCNT (red contour).

375 for the Sn atom, and at 31, 54, 72, 124, 150, 174, 192  $\text{cm}^{-1}$  for the Se atom. Therefore, one can  
 376 conclude that the phonon DOS of the standalone  $\text{Sn}_4\text{Se}_4$  nanowire distinguishes from the bulk  
 377 crystal with several specific vibrational signatures appearing around 30, 54 and 150  $\text{cm}^{-1}$  and pos-  
 378 sibly recognizable in the experiment.

379 On the other hand, the vibrational frequencies at  $\Gamma$  point for the  $\text{Sn}_4\text{Se}_4$  and  $\text{Sn}_6\text{Se}_6$  1D nanowires  
 380 are compiled in Table 2 for the HSE functional. In the case of the  $\text{Sn}_4\text{Se}_4$  wire, the calculated fre-  
 381 quencies are within 7 - 12  $\text{cm}^{-1}$  (i.e. either downshifted or upshifted) with respect to the observed  
 382 ones in the spectra of the two SnSe@SWCNT samples. The modes computed at 181 and 194  $\text{cm}^{-1}$

383 are pure radial SnSe breathing vibrations related to an experimental line appearing between 185  
 384 and 187  $\text{cm}^{-1}$  with relatively strong intensity in the Raman spectrum of filled samples.

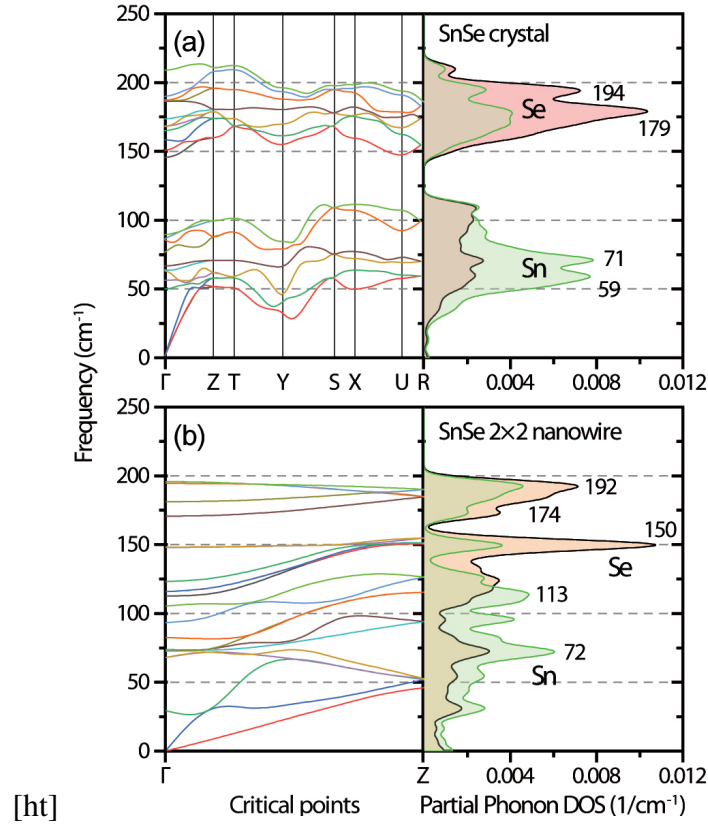


**Figure 6:** Calculated phonon dispersions and density of states of SnSe crystals: (a) 3D  $Pnma$  crystal; (b) 1D  $p4_2/mmc$   $\text{Sn}_4\text{Se}_4$  crystal with dominating flat bands.

385 The computed phonon DOS  $\rho_{1D}$  for the  $\text{Sn}_4\text{Se}_4$  wire shows several features at 117, 150, 174, and  
 386 192  $\text{cm}^{-1}$  which are near the additional Raman lines found in experimental spectra (Fig. 6(b)). The  
 387 phonon DOS shows that the heavier Sn atoms and the lighter Se atoms contribute mainly to the  
 388 acoustic and optical modes, respectively. In particular, the maximum DOS at 150 and 192  $\text{cm}^{-1}$   
 389 corresponds to unique flat bands of the phonon dispersion dominated by Se atoms which may lead  
 390 to low lattice thermal conductivity in the  $\text{Sn}_4\text{Se}_4$  nanowire due to the anharmonic scattering of  
 391 phonons. Meanwhile the group velocity along  $\Gamma$ -Z direction seems lower in the  $\text{Sn}_4\text{Se}_4$  nanowire  
 392 than in the bulk, consistent with flattening of the phonon dispersion curves in this nanowire. In the  
 393 case of the  $\text{Sn}_6\text{Se}_6$  wire, there is also a very good match between calculated and experimental Ra-  
 394 man frequencies at the zone center (Table 2).

**Table 2:** Calculated  $\Gamma$ -point frequencies ( $\text{cm}^{-1}$ ) for  $\text{Sn}_4\text{Se}_4$  and  $\text{Sn}_6\text{Se}_6$  nanowires.

$\text{Sn}_4\text{Se}_4$ ( $2 \times 2$ )								
$A_{1g}$	$A_{2g}$	$B_{1g}$	$B_{2g}$	$E_g$	$A_{2u}$	$B_{1u}$	$B_{2u}$	$E_u$
	29	73	83	68			93	74
					105			
113				116			123	
	148		148					
								171
181		194						196
$\text{Sn}_6\text{Se}_6$								
$A_{1g}$	$A_{2g}$	$B_{2g}$	$E_{1g}$	$E_{2g}$	$A_{2u}$	$B_{1u}+B_{2u}$	$E_{1u}$	$E_{2u}$
	22							
	83		83					90
		121		108		112	110	
				135	135		132	
163		186	172	150		162		181
						230		222
246				254				

395 The highest calculated Raman frequencies at the HSE level occur at 194 ( $B_{1g}$ ) and 254  $\text{cm}^{-1}$  ( $B_{2g}$ )  
396 for the  $\text{Sn}_4\text{Se}_4$  and  $\text{Sn}_6\text{Se}_6$  wires, respectively, while the highest experimental Raman frequency not  
397 assignable to SWCNTs is found at 235  $\text{cm}^{-1}$  in the Raman spectrum of one of the  $\text{SnSe@SWCNT}$   
398 composites. Regarding this band, we note also that phonon calculation of a trigonal-Se crystal with  
399 fixed cell parameters using PBE and HSE06 functionals gives a Raman active mode at 227  $\text{cm}^{-1}$ ,  
400 and 236  $\text{cm}^{-1}$ , respectively, close to the experimental value at 235  $\text{cm}^{-1}$  ( $A_1$  mode) [49,50]. De-  
401 spite that this Raman band observed at 235  $\text{cm}^{-1}$  might be the signature of t-Se presence in the  
402 samples [51,52], there is no other analytical evidence of this material in the composite or of its for-  
403 mation above the melting point of SnSe during the synthesis process. Therefore, we ascribe the 235  
404  $\text{cm}^{-1}$  line to  $\text{Sn}_6\text{Se}_6$  embedded nanowires.

405 Finally, the phonon dispersion in the 3D SnSe crystal shows a phonon gap of about 50  $\text{cm}^{-1}$  in  
406 all directions of the BZ with phonon branches clearly segregated into two groups of frequencies  
407 centered at 70 and 180  $\text{cm}^{-1}$  (Fig. 6(a)). By comparison, the phonon branches of the 1D  $\text{Sn}_4\text{Se}_4$   
408 nanowire do not extend beyond 200  $\text{cm}^{-1}$  with a phonon gap of about 20  $\text{cm}^{-1}$  along  $\Gamma$ -Z between  
409 150 and 175  $\text{cm}^{-1}$  (Fig. 6(b)). While the phonons energies at  $q > 0$  in the  $\text{Sn}_6\text{Se}_6$  nanowire could

410 not be calculated at HSE level with FD method due to limitations stemming from the large size of  
 411 the supercell, the  $q = 0$  phonons frequencies have been determined and are reported in Table 2.  
 412 The absence of negative frequencies in the vibrational calculations and phonon dispersion relations  
 413 shows that the standalone 1D nanowires  $\text{Sn}_4\text{Se}_4$  and  $\text{Sn}_6\text{Se}_6$  are structurally stable.

### 414 3.5 Nanotube-nanowire interaction

415 To estimate the nanotube interaction with the encapsulated SnSe crystals we considered the case  
 416 of the embedded  $\text{Sn}_6\text{Se}_6$  nanowire. The cross section of the DFT optimized standalone  $\text{Sn}_6\text{Se}_6$   
 417 crystal is systematically expanded compared to the crystal diameter of  $\sim 6.2 \text{ \AA}$  revealed by HRTEM.  
 418 In fact, the  $\text{Sn}_6\text{Se}_6$  crystals can fit into (9,9) tubes of  
 419 1.22 nm diameter, which infers for a substantial compressive stress on the  $\text{Sn}_6\text{Se}_6$  crystal as the Se  
 420 distance to the SWCNT wall is  $\sim 3.0 \text{ \AA}$ , i.e. smaller than the sum of Sn and C van der Waals radii  
 421  $\sim 3.5 \text{ \AA}$ .

**Table 3:** Lennard-Jones parameters of  $\text{Se} \cdots \text{C}$  interaction. Forces on the Se atom in the composite  $\text{SnSe@SWCNT}(9,9)$  and on the  $\text{Sn}_6\text{Se}_6$  standalone nanowire after optimization (in  $\text{eV/\AA}$ ).

		Cartesian coordinates of forces			Cross-section
		$x$	$y$	$z$	$\sigma \text{ (\AA)}$
	$\text{Sn}_6\text{Se}_6$	-0.00044	0	0	7.302
[ht]	Se in (9,9) tube	0.48822	0.02555	-0.00259	
		Lennard-Jones parameters			Distance
		$E \text{ (eV)}$	$r_0 \text{ (\AA)}$	$R_{\min} - R_{\max} \text{ (\AA)}$	$d \text{ (\AA)}$
	$\text{Se} \cdots \text{C}$	0.020	3.52	0.5 – 10	2.98

422 To estimate the nanotube interaction with the encapsulated  $\text{Sn}_6\text{Se}_6$  crystal, we derived a simple  
 423 model involving a Lennard-Jones (LJ) potential for a pair of non-bonded Se and C atoms:

$$424 \quad V(r) = -\epsilon \left[ (r_0/r)^{12} - 2(r_0/r)^6 \right] \quad (12)$$

425 where  $\epsilon$  corresponds to the cohesion energy, and  $r_0$  - to the equilibrium distance between the  
 426 atoms, which is usually taken as a sum of their van der Waals radii. Due to the two-body and short-  
 427 range nature of LJ interaction, it is sufficient to calculate on a single protruding Se atom the resul-

428 tant force applied by a finite segment of a (9,9) SWCNT (5 unit cells in our case). The as calcu-  
429 lated force on Se atoms was compared to that exerted on the Se atom in a Sn<sub>6</sub>Se<sub>6</sub> crystal during  
430 optimization *in vacuo*. We established that for realistic Se···C interaction parameters (Table 3)  
431 the intra-nanowire expansion force obtained from the DFT calculations for the standalone Sn<sub>6</sub>Se<sub>6</sub>  
432 1D crystal is compensated by a repulsive LJ force of 0.488 eV/Å at a distance of ~2.98 Å between  
433 the Se atoms and the SWCNT wall. This fact evidences that although Sn<sub>6</sub>Se<sub>6</sub> is stable in vacuo,  
434 its geometry in encapsulated form is influenced by the pressure exerted from the surrounding  
435 SWCNT. On the other hand, the force constant corresponding to the LJ interaction, being of or-  
436 der of  $72\epsilon/r_0^2 \approx 0.116 \text{ eV/\AA}^2$ , is too small to affect significantly the vibrational frequencies of the  
437 Sn<sub>6</sub>Se<sub>6</sub> crystal, where typical Sn-Se force constants are more than an order of magnitude larger.  
438 Therefore, the normal mode analysis based on DFT calculations for the standalone crystal is repre-  
439 sentative for the encapsulated crystal, as well.

## 440 4 Conclusion

441 We have performed a combined experimental and theoretical study of SnSe@SWCNT compos-  
442 ites where periodic DFT calculations support the Raman spectra recorded on several samples. At  
443 the HSE level of theory, the Sn<sub>4</sub>Se<sub>4</sub> 1D crystal exhibits a direct gap larger than that of the 3D crys-  
444 tal allowing direct optical excitations in the near infrared. In contrast, the band structure of the 1D  
445 hexagonal crystal is typical to that of a semimetal due to the overlap at the Fermi level of the upper  
446 valence band and the lower conduction band with small density of states at the Fermi energy. The  
447 calculated vibrational frequencies of the two standalone 1D SnSe nanowires are consistent with  
448 supplemental Raman lines observed in the Raman spectra of SnSe@SWCNT composites. Addi-  
449 tionally, Raman experiments show that the encapsulated SnSe nanowires modify the electronic and  
450 vibrational properties of the surrounding SWCNT walls.

## 451 **Supporting Information**

452 Supporting Information File 1:

453 File Name: snse-nano\_SI.pdf

454 File Format: PDF

455 Title: Workfunction and projected electronic density of states of the stand-alone tin selenide  
456 nanowires.

## 457 **Acknowledgements**

458 We acknowledge Dr. C. Ewels for helpful discussions. This work was supported by the French-  
459 Bulgarian bilateral exchange program through Campus France PHC RILA Grants No. 38661ZF  
460 and No. DHTC France 01/10/09.05.2017 and by Contract No. KP-06-N38/10/6.12.2019 of the  
461 Bulgarian National Science Fund; and by the NATO SPS MYP program N° 985481 “Quantum  
462 sensor”. JS is indebted to the EPSRC for additional support from EPSRC Grants EP/I033394/1  
463 and EP/R019428/1. This research used resources of Centre de Calcul Intensif des Pays de la Loire  
464 (CCIPL), Nantes, France.

## 465 **ORCID iDs**

466 N Kalashnyk <https://orcid.org/0000-0003-0314-6091>

467 E Faulques <https://orcid.org/0000-0002-7761-8509>

468 J. Sloan <https://orcid.org/0000-0001-8612-7456>

469 V G Ivanov <https://orcid.org/0000-0001-5405-8847>

## 470 **References**

- 471 1. Zhang, C.; Yan, Y.; Sheng Zhao, Y.; Yao, J. *Annu. Rep. Prog. Chem., Sect. C: Phys. Chem.*  
472 **2013**, *109*, 211. doi:10.1039/c3pc90002a.
- 473 2. Dasgupta, N. P.; Sun, J.; Liu, C.; Brittman, S.; Andrews, S. C.; Lim, J.; Gao, H.; Yan, R.;  
474 Yang, P. *Adv. Mater.* **2014**, *26* (14), 2137–2184. doi:10.1002/adma.201305929.

- 475 3. Velea, A.; Opsomer, K.; Devulder, W.; Dumortier, J.; Fan, J.; Detavernier, C.; Jurczak, M.;  
476 Govoreanu, B. *Sci Rep* **2017**, 7 (1), 8103. doi:10.1038/s41598-017-08251-z.
- 477 4. Matthews, P. D.; McNaughter, P. D.; Lewis, D. J.; O'Brien, P. *Chem. Sci.* **2017**, 8 (6),  
478 4177–4187. doi:10.1039/C7SC00642J.
- 479 5. Jing, Y.; Liu, B.; Zhu, X.; Ouyang, F.; Sun, J.; Zhou, Y. *Nanophotonics* **2020**, 9 (7),  
480 1675–1694. doi:doi:10.1515/nanoph-2019-0574.
- 481 6. Jia, T.; Feng, Z.; Guo, S.; Zhang, X.; Zhang, Y. *ACS Appl. Mater. Interfaces* **2020**, 12 (10),  
482 11852–11864. doi:10.1021/acsami.9b23297.
- 483 7. Gao, M.-R.; Xu, Y.-F.; Jiang, J.; Yu, S.-H. *Chem. Soc. Rev.* **2013**, 42 (7), 2986. doi:10.1039/  
484 c2cs35310e.
- 485 8. Shi, W.; Gao, M.; Wei, J.; Gao, J.; Fan, C.; Ashalley, E.; Li, H.; Wang, Z. *Adv. Sci.* **2018**, 5  
486 (4), 1700602. doi:10.1002/advs.201700602.
- 487 9. Zhao, L.-D.; Lo, S.-H.; Zhang, Y.; Sun, H.; Tan, G.; Uher, C.; Wolverton, C.; Dravid, V. P.;  
488 Kanatzidis, M. G. *Nature* **2014**, 508 (7496), 373–377. doi:10.1038/nature13184.
- 489 10. Kumar, M.; Rani, S.; Singh, Y.; Gour, K. S.; Singh, V. N. *RSC Adv.* **2021**, 11, 6477–6503.  
490 doi:10.1039/D0RA09807H.
- 491 11. Saito, R.; Dresselhaus, G.; Dresselhaus, M. S. *Physical Properties of Carbon Nanotubes*;  
492 Published by Imperial College and distributed by World Scientific Publishing Co., 1998;  
493 doi:10.1142/p080.
- 494 12. Ajayan, P. M.; Zhou, O. Z. *Applications of Carbon Nanotubes In: Dresselhaus M.S., Dres-*  
495 *selhaus G., Avouris P. (eds) Carbon Nanotubes. Topics in Applied Physics, vol 80; Springer,*  
496 *Berlin, Heidelberg, 2001; doi:10.1007/3-540-39947-X\_14.*
- 497 13. Schnorr, J. M.; Swager, T. M. *Chemistry of Materials* **2011**, 23 (3), 646–657. doi:10.1021/  
498 cm102406h.

- 499 14. Carter, R.; Sloan, J.; Kirkland, A. I.; Meyer, R. R.; Lindan, P. J. D.; Lin, G.; Green, M. L. H.;  
500 Vlandas, A.; Hutchison, J. L.; Harding, J. *Phys. Rev. Lett.* **2006**, *96*, 215501. doi:10.1103/  
501 PhysRevLett.96.215501.
- 502 15. Giusca, C. E.; Stolojan, V.; Sloan, J.; Börrnert, F.; Shiozawa, H.; Sader, K.; Rümmeli, M. H.;  
503 Büchner, B.; Silva, S. R. P. *Nano Lett.* **2013**, *13* (9), 4020–4027. doi:10.1021/nl4010354.  
504 PMID: 23984706
- 505 16. Carter, R.; Suyetin, M.; Lister, S.; Dyson, M. A.; Trehwitt, H.; Goel, S.; Liu, Z.; Suenaga, K.;  
506 Giusca, C.; Kashtiban, R. J.; Hutchison, J. L.; Dore, J. C.; Bell, G. R.; Bichoutskaia, E.;  
507 Sloan, J. *Dalton Trans.* **2014**, *43* (20), 7391–7399. doi:10.1039/C4DT00185K.
- 508 17. Nagata, M.; Shukla, S.; Nakanishi, Y.; Liu, Z.; Lin, Y.-C.; Shiga, T.; Nakamura, Y.;  
509 Koyama, T.; Kishida, H.; Inoue, T.; Kanda, N.; Ohno, S.; Sakagawa, Y.; Suenaga, K.; Shino-  
510 hara, H. *Nano letters* **2019**, *19* (8), 4845—4851. doi:10.1021/acs.nanolett.8b05074.
- 511 18. Slade, C. A.; Sanchez, A. M.; Sloan, J. *Nano Lett.* **2019**, *19* (5), 2979–2984. doi:10.1021/acs.  
512 nanolett.9b00133.
- 513 19. Lin, J.; Cretu, O.; Zhou, W.; Suenaga, K.; Prasai, D.; Bolotin, K. I.; Cuong, N. T.; Otani, M.;  
514 Okada, S.; Lupini, A. R.; Idrobo, J.-C.; Caudel, D.; Burger, A.; Ghimire, N. J.; Yan, J.; Man-  
515 drus, D. G.; Pennycook, S. J.; Pantelides, S. T. *Nature Nanotechnology* **2014**, *9* (6), 436–442.  
516 doi:10.1038/nnano.2014.81.
- 517 20. Koh, A. L.; Wang, S.; Ataca, C.; Grossman, J. C.; Sinclair, R.; Warner, J. H. *Nano Letters*  
518 **2016**, *16* (2), 1210–1217. doi:10.1021/acs.nanolett.5b04507. PMID: 26785319
- 519 21. Çakır, D.; Durgun, E.; Gülseren, O.; Ciraci, S. *Phys. Rev. B* **2006**, *74*, 235433. doi:10.1103/  
520 PhysRevB.74.235433.
- 521 22. Murugan, P.; Kumar, V.; Kawazoe, Y.; Ota, N. *Nano Letters* **2007**, *7* (8), 2214–2219. doi:10.  
522 1021/nl0706547. PMID: 17625902

- 523 23. Spencer, J. H.; Nesbitt, J. M.; Trehitt, H.; Kashtiban, R. J.; Bell, G.; Ivanov, V. G.;  
524 Faulques, E.; Sloan, J.; Smith, D. C. *ACS Nano* **2014**, 8 (9), 9044–9052. doi:10.1021/  
525 nn5023632.
- 526 24. Ivanov, V. G.; Kalashnyk, N.; Sloan, J.; Faulques, E. *Phys. Rev. B* **2018**, 98 (12), 125429. doi:  
527 10.1103/PhysRevB.98.125429.
- 528 25. Clark, S. J.; Segall, M. D.; Pickard, C. J.; Hasnip, P. J.; Probert, M. I. J.; Refson, K.;  
529 Payne, M. C. *Zeitschrift für Kristallographie - Crystalline Materials* **2005**, 220 (5/6), year.  
530 doi:10.1524/zkri.220.5.567.65075.
- 531 26. Hummer, K.; Harl, J.; Kresse, G. *Phys. Rev. B* **2009**, 80 (11), 115205. doi:10.1103/PhysRevB.  
532 80.115205.
- 533 27. Clark, S. J.; Robertson, J. *Phys. Rev. B* **2010**, 82 (8), 085208. doi:10.1103/PhysRevB.82.  
534 085208.
- 535 28. Kim, B. G.; Jo, J.; Cheong, S. *Journal of Solid State Chemistry* **2013**, 197, 134–138. doi:https:  
536 //doi.org/10.1016/j.jssc.2012.08.047.
- 537 29. Andriotis, A. N.; Richter, E.; Menon, M. *Phys. Rev. B* **2016**, 93, 081413. doi:10.1103/  
538 PhysRevB.93.081413.
- 539 30. Okazaki, A.; Ueda, I. *Journal of the Physical Society of Japan* **1956**, 11 (4), 470–470. doi:10.  
540 1143/JPSJ.11.470.
- 541 31. Kroumova, E.; Aroyo, M. I.; Perez-Mato, J. M.; Kirov, A.; Capillas, C.; Ivantchev, S.;  
542 Wondratschek, H. *Phase Transitions* **2003**, 76 (1-2), 155–170. doi:10.1080/  
543 0141159031000076110.
- 544 32. Das, A.; Kumar, A.; Banerji, P. *Journal of Physics: Condensed Matter* **2020**, 32 (26), 265501.  
545 doi:10.1088/1361-648x/ab7ad8.

- 546 33. Yan, J.; Ke, F.; Liu, C.; Wang, L.; Wang, Q.; Zhang, J.; Li, G.; Han, Y.; Ma, Y.; Gao, C. *Phys.*  
547 *Chem. Chem. Phys.* **2016**, *18* (6), 5012–5018. doi:10.1039/C5CP07377D.
- 548 34. Kharlamova, M. V. *Journal of Spectroscopy* **2015**, *2015*, 1–8. doi:10.1155/2015/653848.
- 549 35. Araujo, P. T.; Maciel, I. O.; Pesce, P. B. C.; Pimenta, M. A.; Doorn, S. K.; Qian, H.;  
550 Hartschuh, A.; Steiner, M.; Grigorian, L.; Hata, K.; Jorio, A. *Phys. Rev. B* **2008**, *77* (24),  
551 241403. doi:10.1103/PhysRevB.77.241403.
- 552 36. Chandrasekhar, H. R.; Humphreys, R. G.; Zwicky, U.; Cardona, M. *Phys. Rev. B* **1977**, *15* (4),  
553 2177–2183. doi:10.1103/PhysRevB.15.2177.
- 554 37. Li, X.-Z.; Xia, J.; Wang, L.; Gu, Y.-Y.; Cheng, H.-Q.; Meng, X.-M. *Nanoscale* **2017**, *9* (38),  
555 14558–14564. doi:10.1039/C7NR05047J.
- 556 38. Xu, X.; Song, Q.; Wang, H.; Li, P.; Zhang, K.; Wang, Y.; Yuan, K.; Yang, Z.; Ye, Y.; Dai, L.  
557 *ACS Appl. Mater. Interfaces* **2017**, *9* (14), 12601–12607. doi:10.1021/acsami.7b00782.
- 558 39. Liu, F.; Parajuli, P.; Rao, R.; Wei, P. C.; Karunaratne, A.; Bhattacharya, S.; Podila, R.; He, J.;  
559 Maruyama, B.; Priyadarshan, G.; Gladden, J. R.; Chen, Y. Y.; Rao, A. M. *Phys. Rev. B* **2018**,  
560 *98* (22), 224309. doi:10.1103/PhysRevB.98.224309.
- 561 40. Xu, H.; Xing, J.; Huang, Y.; Ge, C.; Lu, J.; Han, X.; Du, J.; Hao, H.; Dong, J.; Liu, H.  
562 *Nanoscale Research Letters* **2019**, *14* (1), 17. doi:10.1186/s11671-019-2850-0.
- 563 41. Kang, M.; Rathi, S.; Lee, I.; Li, L.; Khan, M. A.; Lim, D.; Lee, Y.; Park, J.; Pham, A. T.;  
564 Duong, A. T.; Cho, S.; Yun, S. J.; Kim, G.-H. *J. nanosci. nanotechnol.* **2018**, *18* (6), 4243–4247.  
565 doi:10.1166/jnn.2018.15189.
- 566 42. Rao, R.; Pierce, N.; Dasgupta, A. *Applied Physics Letters* **2014**, *105* (7), 073115. doi:10.1063/  
567 1.4893698.
- 568 43. Zafar, Z.; Zafar, A.; Tian, Y.; Cao, Z.; Jin, B.; Shi, Z. *Journal of Raman Spectroscopy* **2017**,  
569 *48* (10), 1318–1322. doi:https://doi.org/10.1002/jrs.5239.

- 570 44. Brown, S. D. M.; Jorio, A.; Corio, P.; Dresselhaus, M. S.; Dresselhaus, G.; Saito, R.;  
571 Kneipp, K. *Phys. Rev. B* **2001**, *63* (15), 155414. doi:10.1103/PhysRevB.63.155414.
- 572 45. Nguyen, K. T.; Gaur, A.; Shim, M. *Phys. Rev. Lett.* **2007**, *98* (14), 145504. doi:10.1103/  
573 PhysRevLett.98.145504.
- 574 46. Gayen, S.; Behera, S. N.; Bose, S. M. *Phys. Rev. B* **2007**, *76*, 165433. doi:10.1103/PhysRevB.  
575 76.165433.
- 576 47. Hasdeo, E. H.; Nugraha, A. R. T.; Dresselhaus, M. S.; Saito, R. *Phys. Rev. B* **2014**, *90* (24),  
577 245140. doi:10.1103/PhysRevB.90.245140.
- 578 48. Luo, X.; Huang, J.; Li, J.; Cao, L.; Cheng, Y.; Guo, L.; Wang, Y.; Qi, H. *Applied Surface Sci-*  
579 *ence* **2019**, *491*, 95–104. doi:https://doi.org/10.1016/j.apsusc.2019.06.129.
- 580 49. Sinha, A. K.; Sasmal, A. K.; Mehetor, S. K.; Pradhan, M.; Pal, T. *Chem. Commun.* **2014**, *50*  
581 (99), 15733–15736. doi:10.1039/C4CC08168D.
- 582 50. Pal, A.; Gohil, S.; Sengupta, S.; Poswal, H. K.; Sharma, S. M.; Ghosh, S.; Ayyub, P. *J. Phys.:  
583 Condens. Matter* **2015**, *27* (41), 415404. doi:10.1088/0953-8984/27/41/415404.
- 584 51. Colin, R.; Drowart, J. *Trans. Faraday Soc.* **1964**, *60*, 673–683. doi:10.1039/TF9646000673.
- 585 52. Vasylenko, A.; Marks, S.; Wynn, J. M.; Medeiros, P. V. C.; Ramasse, Q. M.; Morris, A. J.;  
586 Sloan, J.; Quigley, D. *ACS Nano* **2018**, *12* (6), 6023–6031. doi:10.1021/acsnano.8b02261.  
587 PMID: 29782147